

ARTICLE OPEN



Changes in global DMS production driven by increased CO₂ levels and its impact on radiative forcing

Junri Zhao¹, Yan Zhang^{1,2,3}✉, Shujun Bie¹, Kelsey R. Billsback^{4,5}, Jeffrey R. Pierce⁴ and Ying Chen¹

Our study highlights the importance of understanding the future changes in dimethyl-sulfide (DMS), the largest natural sulfur source, in the context of ocean acidification driven by elevated CO₂ levels. We found a strong negative correlation ($R^2 = 0.89$) between the partial pressure of carbon dioxide (pCO₂) and sea-surface DMS concentrations based on global observational datasets, not adequately captured by the Coupled Model Intercomparison Project Phase 6 (CMIP6) Earth System Models (ESMs). Using this relationship, we refined projections of future sea-surface DMS concentrations in CMIP6 ESMs. Our study reveals a decrease in global sea-surface DMS concentrations and the associated aerosol radiative forcing compared to ESMs' results. These reductions represent ~9.5% and 11.1% of the radiative forcings resulting from aerosol radiation and cloud interactions in 2100 reported by the Intergovernmental Panel on Climate Change Sixth Assessment Report. Thus, future climate projections should account for the climate implications of changes in DMS production due to ocean acidification.

npj *Climate and Atmospheric Science* (2024)7:18; <https://doi.org/10.1038/s41612-024-00563-y>

INTRODUCTION

DMS, as the predominant volatile sulfur compound residing in the upper ocean surface, assumes a pivotal role in the regulation of Earth's climate^{1,2}. Upon its release into the atmosphere, DMS undergoes oxidation, giving rise to the formation of SO₄²⁻ particles. These particles directly reflect solar radiation and also act as cloud condensation nuclei (CCN), manipulating the radiative properties of clouds and thereby inducing a subsequent cooling effect on Earth's surface temperatures^{3,4}. The Intergovernmental Panel on Climate Change (IPCC) Sixth Assessment Report (AR6)⁵ reveals that future scenarios project a substantial absorption of 38–70% of CO₂ emissions by oceans and land by the end of the 21st century. This absorption is anticipated to lead to a significant reduction in ocean pH, resulting in profound consequences for marine biological processes and potentially influencing DMS production. Therefore, it is crucial to incorporate the mechanisms underlying the response of DMS production to ocean acidification (OA) in order to furnish reliable projections of DMS emissions.

Numerous mesocosm studies^{6–11} have contributed to enhancing our understanding of the response of DMS production to ocean acidification (OA), indicating that sea-surface DMS concentrations tend to decrease in the presence of high CO₂/low pH conditions. However, the relationship between pH (pCO₂) and algal DMS production, as well as DMS decomposition, is intricate¹². Some studies^{13,14} have indicated that a decrease in pH can lead to reduced DMS production by affecting the phytoplankton responsible for DMSP production (the primary precursor of DMS), but cases where DMSP production remained unaffected have been reported¹⁵. Six et al.¹⁶ utilized the correlation between sea-surface DMS concentrations and pH to project future global DMS emissions and associated radiative forcing. State-of-the-art Earth System Models (ESMs) have incorporated mechanisms to simulate the response of DMS

production to OA, some^{17,18} directly employing parameterization schemes proposed by Six et al.¹⁶. Nevertheless, the predictive capacity of this relationship in ESMs has not been evaluated due to inadequate observational coverage¹⁹ of biogeochemical variables. Furthermore, the current generation of ESMs exhibits limitations in accurately constraining marine productivity²⁰, which can restrict their ability to precisely predict the response of DMS production to OA.

This study aims to evaluate the future trajectory of global sea-surface DMS concentrations within the context of ocean acidification driven by elevated CO₂ levels, as well as to investigate their impact on aerosol radiative forcing. To accomplish this, we established a robust relationship between sea-surface DMS and pCO₂ (a critical indicator of ocean acidification) using comprehensive observational datasets spanning a global scale. This relationship was then employed to refine the sea-surface DMS concentration outputs derived from multiple models participating in the Coupled Model Intercomparison Project Phase 6 (CMIP6)²¹. Consequently, we generated projections of global sea-surface DMS concentrations from 2020 to 2099 under the socio-economic Pathway (SSP) 5-8.5 scenario²². Furthermore, we quantified the radiative forcing induced by DMS by integrating an advanced aerosol microphysics model with a global 3D-chemical transport model driven by meteorology data for the SSP5-8.5 future scenario.

RESULTS

The relationship between pCO₂ and DMS and the projection method

We observed a strong negative correlation between sea-surface pCO₂ and DMS across the global ocean, with an R^2 value of 0.89 (Fig. 1a). The matched data, as described in "Methods", were

¹Shanghai Key Laboratory of Atmospheric Particle Pollution and Prevention (LAP3), National Observations and Research Station for Wetland Ecosystems of the Yangtze Estuary, Department of Environmental Science and Engineering, Fudan University, 200438 Shanghai, China. ²Shanghai Institute of Eco Chongming (SIEC), 200062 Shanghai, China. ³MOE Laboratory for National Development and Intelligent Governance, Shanghai Institute for Energy and Carbon Neutrality Strategy, IRDR ICoE on Risk Interconnectivity and Governance on Weather/Climate Extremes Impact and Public Health, Fudan University, 200433 Shanghai, China. ⁴Department of Atmospheric Science, Colorado State University, Fort Collins, CO, USA. ⁵PSE Healthy Energy, Oakland, CA, USA. ✉email: yan_zhang@fudan.edu.cn

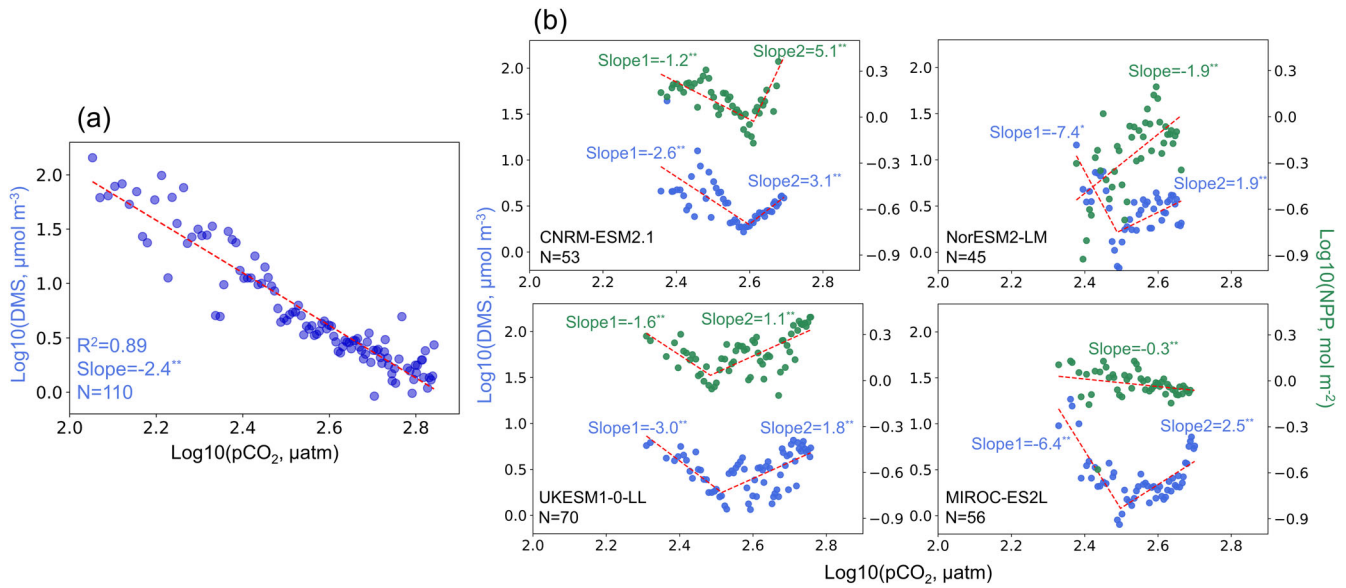


Fig. 1 Assessment of pCO₂ and DMS relationships in ESMs. The scatter plot of pCO₂ and DMS measurements across the global ocean (a), and four ESMs estimated monthly oceanic pCO₂, DMS concentrations, and NPP (b). The red dashed lines indicate the linear regressions between pCO₂ and DMS, as well as pCO₂ and NPP, as estimated by the ESMs. Significant trends are marked by asterisks (* for $P < 0.05$ and ** for $P < 0.01$). The values of trends are evaluated using the Mann–Kendall test. R^2 , Slope, and N represent Pearson's correlation coefficient, the slope of the regression line, and the number of data points.

subsequently partitioned into two groups based on seawater location in the Northern and Southern hemispheres, as illustrated in Supplementary Fig. 2a, b. Notably, the strength of the anti-correlation is relatively weaker for the Northern hemisphere ($R^2 = 0.40$) compared to the Southern hemisphere ($R^2 = 0.87$). In the Northern hemisphere, there are significantly higher nutrient inputs compared to the Southern hemisphere, and regions downstream of densely populated areas exhibit elevated deposition rates^{23,24}. We postulated that these factors contribute to a broader range of fluctuations in DMS concentrations in the Northern Hemisphere due to increased human activities. The plot displaying the correlation between remotely sensed climatological chlorophyll (Chl) data and changes in DMS measurements (Supplementary Fig. 2c, d) reveals that the correlation is lower in the Northern Hemisphere ($R^2 = 0.23$) compared to the Southern Hemisphere ($R^2 = 0.53$). In addition, within the same range of DMS concentration changes ($\text{Log}_{10}(\text{DMS}): 0\text{--}0.7$), corresponding Chl concentration fluctuations in the Northern Hemisphere are more significant compared to those in the Southern Hemisphere. However, due to discrepancies between satellite-derived Chl concentrations and in-situ Chl data, satellite-based Chl data may weaken the relationship between Chl and DMS²⁵.

We devised a projection method based on the relationship derived from Fig. 1a and applied it to improve the estimation of sea-surface DMS concentrations provided by CMIP6 ESMs under the SSP5-8.5 future scenario. In this method, we calculated the changes in model-predicted oceanic $\text{Log}_{10}(\text{pCO}_2)$ (ΔpCO_2) and $\text{Log}_{10}(\text{DMS})$ (ΔDMS) for each specific month (e.g., from January 1st of the current year to January 1st of the previous year). For each grid cell, if the ratio of ΔDMS to ΔpCO_2 exceeded the regression slope defined in Supplementary Eq. (11), we refined ΔDMS by multiplying the slope from Supplementary Eq. (11) by ΔpCO_2 . Conversely, when this ratio fell below the specified threshold, we retained the ΔDMS estimates derived directly from the ESMs. For a detailed description of the projection equations (Supplementary Eqs. (2)–(5)), please refer to the accompanying Supplementary Methods.

Evaluation of CMIP6 ESMs against to observations

Concerning the four ESMs (Supplementary Table 1) utilized in this study, all of them took into account the influence of ocean acidification on marine chemistry²⁶. Nevertheless, it's worth noting that only CNRM-ESM2-1's simulations account for the influence of pH changes on DMS production, as per the straightforward parameterization scheme initially proposed by Six et al.¹⁶ (refer to Supplementary Methods). To validate the application of the fitted relationship in refining future DMS changes, we assessed the ability of the four CMIP6 ESMs to capture the relationship between pCO₂ and DMS changes depicted in Fig. 1a. Figure 1b displays the pCO₂ and oceanic DMS concentrations estimated by these models, corresponding to the same temporal and spatial coordinates as the measurement data in Fig. 1a. Nonetheless, our study found that all four ESMs used encounter challenges when attempting to replicate the observed relationship between pCO₂ and DMS concentrations.

CNRM-ESM2-1²⁷ incorporates prognostic DMS parameterizations, allowing it to simulate the biological processes associated with the release of DMS precursors into seawater and the subsequent DMS sinks. In our quest to dissect the role of biology in influencing DMS concentration changes, we turn our attention to marine net primary productivity (NPP). Figure 1b illustrates that the trend in NPP closely parallels the trend of DMS in response to pCO₂ changes for CNRM-ESM2-1. This implies that the parameterization in CNRM-ESM2-1, which incorporates pH-dependent constraints, might not sufficiently constrain the response of DMS production to pH changes, indicating a need for further refinement to more accurately represent this process. NorESM2-LM¹⁸ also employs prognostic DMS parameterizations. However, DMS in NorESM2-LM is directly released into the water and is computed as a function of temperature and simulated detritus export production. Due to this approach, the trend in NPP does not explicitly align with the trend of DMS in response to pCO₂ changes for NorESM2-LM. In the case of UKESM1-0-LL²⁸, a simpler empirical parameterization is used to simulate oceanic DMS, which is based on chlorophyll, light, and a nutrient term. Chlorophyll and nutrient are considered the primary indicator of

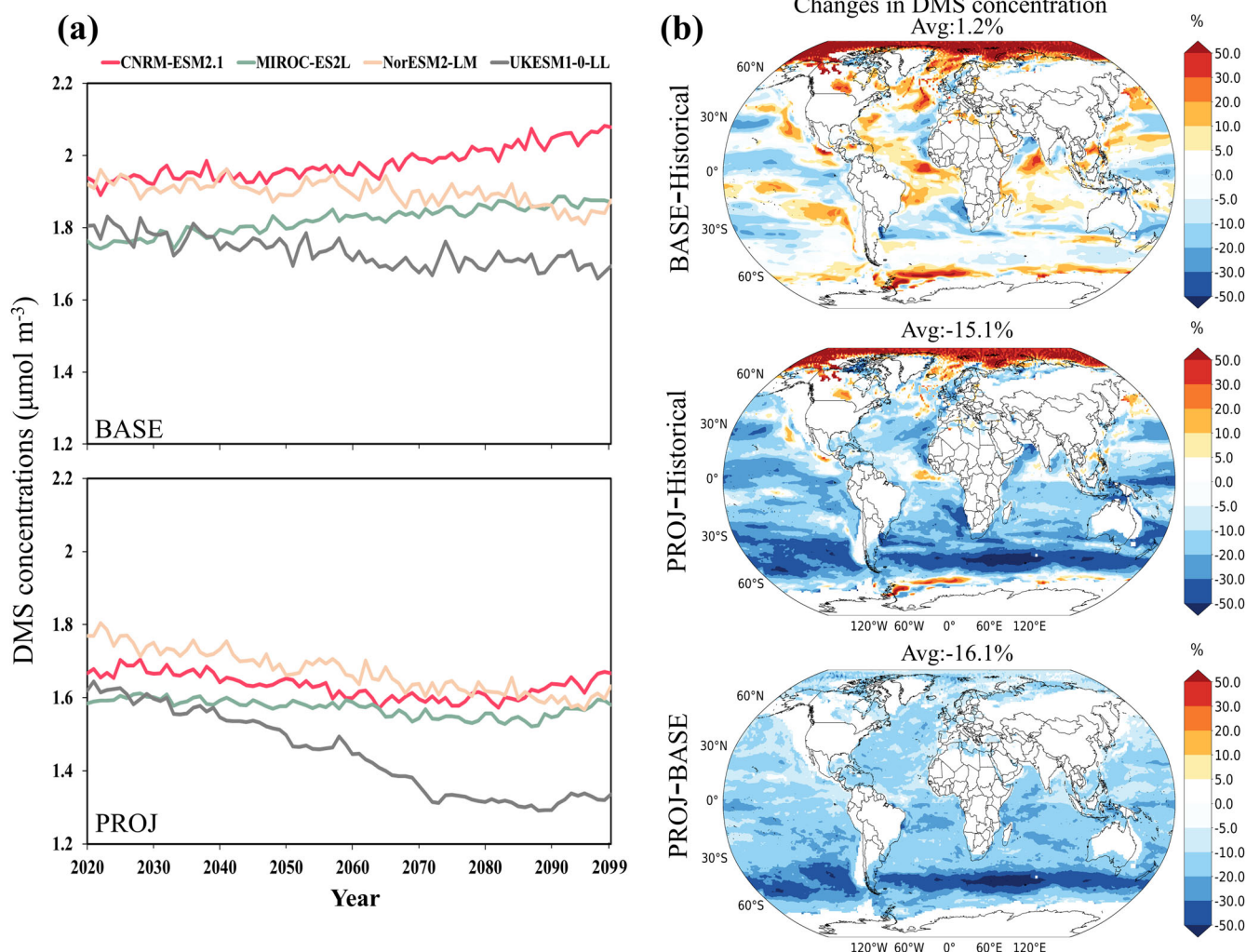


Fig. 2 Comparisons of sea-surface DMS concentrations estimated by four CMIP6 ESMs (BASE) and those projected in this study (PROJ). The time series of global annual mean sea-surface DMS concentrations between 2020 and 2099 under SSP5-8.5 scenario (a). Spatial distributions of changes in the sea-surface DMS concentrations ($1^\circ \times 1^\circ$) among the results of Historical, BASE, and PROJ (b). Historical represent the Averaged sea-surface DMS concentrations from CMIP6 ESMs Historical experiments, 1960–2014.

surface ocean primary production. Consequently, the trend in NPP closely mirrors the trend of DMS in response to $p\text{CO}_2$ changes for UKESM1-0-LL. In contrast, MIROC-ES2L²⁹ exhibits no clear correlation between DMS and NPP. This may be attributed to the parameterization of Aranami and Tsunogai³⁰ used, as indicated in Bock et al.'s²⁰ analysis.

Prospective trends in DMS concentration and flux

Figure 2a presents the trends in global annual mean sea-surface DMS concentration as estimated by four CMIP6 ESMs (BASE) and the refined projections from this study (PROJ) for the period 2020–2099 under the SSP5-8.5 scenario. The PROJ results demonstrate a consistent decrease in sea-surface DMS concentration across all four ESMs throughout the entire period from 2020 to 2099. Specifically, by the end of the century (2099), the global mean sea-surface DMS concentration in PROJ exhibits a substantial decline of 15.1% (with a range of 7.0–26.3%) compared to the Historical results (average of the historical period spanning from 1960 to 2014). In contrast, the BASE results exhibit diverse trends primarily influenced by variations in the DMS parameterization schemes employed by the four ESMs, leading to disparities in the projected direction of the trend. The global mean sea-

surface DMS concentration in BASE shows a marginal increase of 1.2% (with a range of -9.5% to 9.5%) in 2099 relative to the Historical results (Supplementary Fig. 3).

We observed a widespread decline in oceanic DMS concentration across almost all ocean regions (PROJ-Historical), as shown by Fig. 2b. The most substantial reduction of 71.3% occurred in the southern hemisphere. In contrast, due to projected sea-ice changes, the Arctic region exhibited an increase of over 50% in DMS concentrations between BASE and Historical (BASE-Historical), as well as PROJ-Historical results. This could be attributed to the retreat of sea ice, which enhances DMS production by increasing light availability for photosynthesis³¹. Prior studies within the CMIP6 model evaluation²⁰ have similarly demonstrated an increase in oceanic DMS concentrations with a decrease in the fraction of sea-ice cover in the Arctic region under the SSP5-8.5 scenario. Examining the global annual mean DMS flux, we observed an 8.7% increase in BASE but a 10.9% decrease in PROJ compared to the Historical results (Fig. 3). The changes in fluxes showed a shift toward positive values (-10.9% to 8.7%), unlike the changes in concentration (-15.1% to 1.2%). This disparity between concentration and emission changes can be mainly attributed to the positive relationship between air-sea exchange

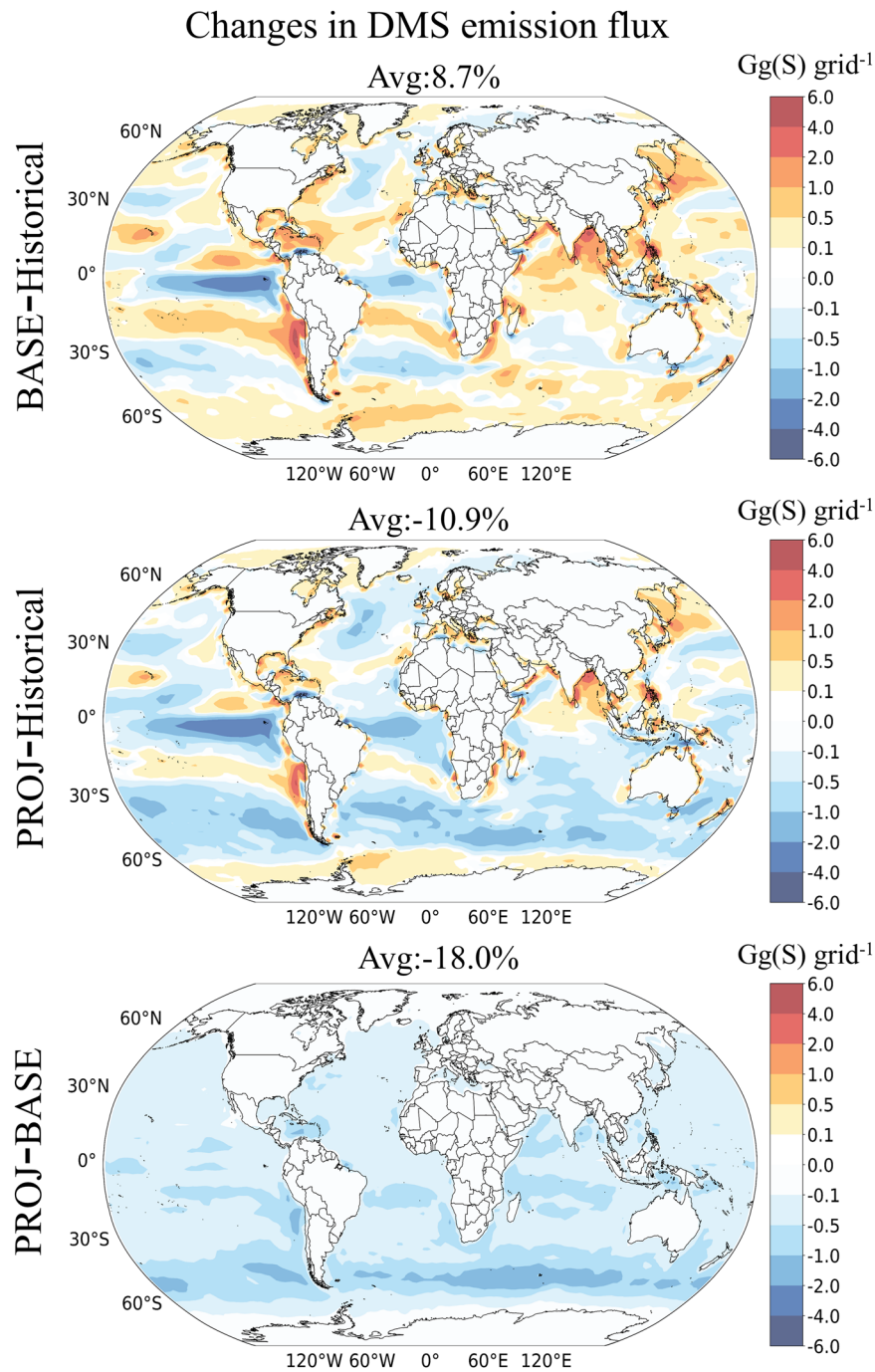


Fig. 3 The spatial distributions of changes in the oceanic DMS emissions fluxes ($2^\circ \times 2.5^\circ$) among the results of Historical, BASE, and PROJ results. The sea-air DMS flux is calculated using the Nightingale et al.⁵⁶ parameterization of gas transfer velocity.

parameterization and sea-surface temperature (Eq. (S6)), which experienced significant increases in 2099 under the SSP5-8.5 scenario²⁰. On a global scale, our projections indicate a decrease of -16.1% in sea-surface DMS concentration and an 18% decline in flux (PROJ-BASE) by 2099 compared to estimates provided by CMIP6 ESMs. For the spatial distribution of annual mean seawater DMS concentrations, please refer to Supplementary Fig. 4.

Prospective changes in DMS-induced radiative forcing

To explore the DMS radiative forcing for 2099 under the SSP5-8.5 scenario, we performed three different annual simulations

(Supplementary Table 2). The REF simulation utilized DMS emissions calculated from averaged sea-surface DMS concentrations (BASE) obtained from four ESMs, the PRD simulation represented DMS emissions based on our projected estimates (PROJ), and the ND simulation had DMS emissions turned off. In 2099, the global mean top-of-atmosphere (TOA) direct radiative forcing (DRF) and cloud-albedo indirect radiative forcing (IRF) induced by DMS decreased 16.4% (from -0.13 to -0.11 W m^{-2}) and 12.1% (from -0.24 to -0.22 W m^{-2}), respectively, when comparing the PRD-ND simulations to the REF-ND simulations (Fig. 4). This decrease corresponds to a reduction of 0.02 W m^{-2} and 0.03 W m^{-2} for DMS-derived DRF and cloud-albedo IRF,

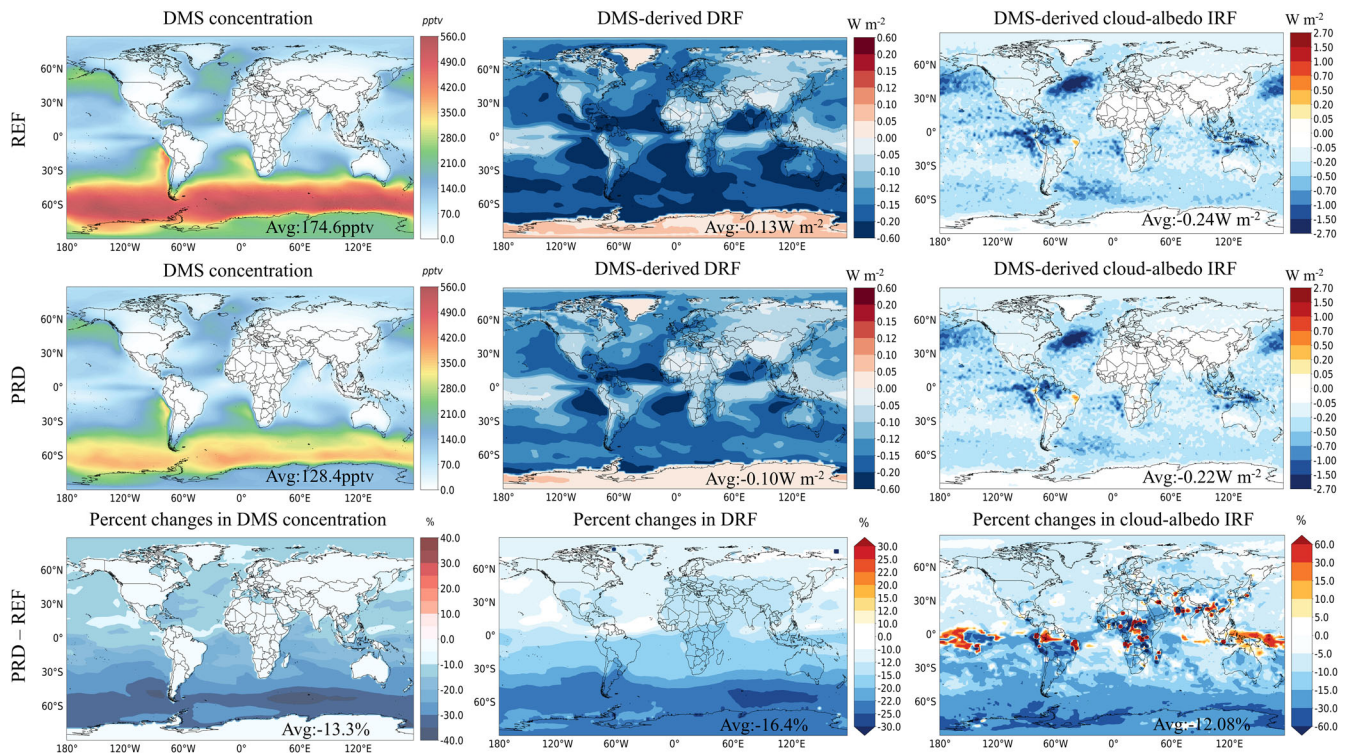


Fig. 4 The simulated atmospheric DMS concentration and DMS-induced radiative forcing in 2099. The first and second row presents the spatial distributions of annual mean atmospheric DMS concentration and its derived all-sky DRF and cloud-albedo IRF in 2099. The third row presents the percent changes in DMS concentration and the magnitude of the all-sky DRF and cloud-albedo IRF between PRD and REF simulations.

representing $\sim 9.5\%$ and 11.1% of the total radiative forcings induced by aerosol radiation interactions and cloud interactions in 2100 under the SSP5-8.5 scenario as reported by AR6 (Table AIII.4e in Full Report⁵). Regions exhibiting higher reductions in atmospheric DMS concentrations (30–40%) from the PRD-REF simulation were primarily located in the high-latitude southern hemisphere, and large decreases in annual mean DRF (20–30%) and IRF (15–60%) were also observed over the high-latitude southern hemisphere.

The average concentrations of SO_4^{2-} and particles with diameters larger than 80 nm (N80, a proxy for CCN-sized particles³²) decreased from $0.25 \mu\text{g m}^{-3}$ to $0.21 \mu\text{g m}^{-3}$ and 39.5% to 36.5% (averaging the percent differences of each grid cell) within the global domain in 2099 between RPD and REF simulations (Supplementary Fig. 5), respectively. The spatial distributions of DRF (Fig. 4) were generally consistent with those of SO_4^{2-} concentrations enhanced by DMS emissions (Supplementary Fig. 5). However, some discrepancies were observed in the distributions of the effects of DMS on IRF and N80. For instance, higher increases in N80 from DMS emissions were observed around the equatorial belt in the Pacific Ocean, which did not directly correlate with stronger negative IRF in those areas. These discrepancies can be attributed to factors such as surface albedo and cloud fractions^{32–34}.

DISCUSSION

The substantial decline observed in global anthropogenic emissions over the past decade³⁵ accentuates the growing significance of natural emissions, including those originating from DMS. Consequently, it becomes imperative to accurately quantify these forthcoming emissions, given their potential implications for climate. In our study, we found that the CMIP6 ESMs did not

adequately capture the relationship between sea-surface pCO_2 and DMS when compared with multi-year and globally distributed observational datasets established in this research. Therefore, further refinement of the future sea-surface DMS concentration estimated by CMIP6 ESMs is necessary. Our findings suggest that if the relationship depicted in Fig. 1a remains applicable under future oceanic conditions, the anticipated rise in anthropogenic CO_2 storage within the ocean could have a substantial impact on DMS concentrations, resulting in a reduction in the magnitude of DMS-induced radiative forcing. Therefore, it is crucial to consider the potential climate implications of changes in DMS production resulting from relative biogeochemical drivers when projecting future climate change.

We acknowledge several limitations in our study. The utilization of two ratios (Supplementary Fig. 2a, b) for the calculation of DMS concentration might be seen as rather simplistic. To investigate the pCO_2 and DMS ratios in different oceanic regions, we conducted a comparative analysis across the global ocean at latitudinal bands of 90° , 60° , 45° , and 30° , as depicted in Supplementary Fig. 6. The results in the 45°S – 0° and 30°S – 0° (Supplementary Fig. 6g, l) regions revealed a relatively higher regression slope (approximately -0.8) in these areas when compared to the high-latitude regions in the Southern Hemisphere (e.g., 90°S – 45°S (f) or 90°S – 60°S (j)), where the slopes ranged from -2.6 to -2.4 . This suggests that the negative trend of DMS in response to pCO_2 changes in the 45°S – 0° and 30°S – 0° regions (Supplementary Fig. 6g, l) is comparatively slower than in the high-latitude Southern Hemisphere regions (Supplementary Fig. 6f, j). Therefore, we re-evaluated the global annual mean sea-surface DMS concentration by applying Equations S2–S5, utilizing four ratios derived from the 45° latitudinal band interval (Supplementary Fig. 6f–i), as these ratios exhibit statistically significant trends ($P < 0.05$). The recalculated annual mean sea-

surface DMS concentrations for the period 2020–2099 indicate a $0.02\text{--}0.06\ \mu\text{mol m}^{-3}$ increase compared to the values computed using two ratios (Supplementary Fig. 7a). Notably, the global mean sea-surface DMS concentration in 2099, employing four ratios, reveals a decrease of 13.3% (ranging from 5.0 to 24.1%) relative to Historical results. This suggests a potential slight underestimation in estimates for DMS emissions and resultant radiative forcing, likely attributable to the use of the Southern Hemisphere's regional average slope (Supplementary Fig. 6a) in the calculations.

However, from Supplementary Fig. 6g, k, l, it can be observed that the range of pCO_2 measurements in this region has a relatively short interval. Therefore, using the results from this region may not fully reflect the response of DMS to significant pCO_2 changes. Furthermore, for the Northern Hemisphere, the results in the $0^\circ\text{--}45^\circ\text{N}$ (h) and $45^\circ\text{N}\text{--}90^\circ\text{N}$ (h) regions, with slopes ranging from -0.8 to -0.6 , are similar to the results in the $0^\circ\text{--}90^\circ\text{N}$ (b) region (-0.7). However, in the $0^\circ\text{--}30^\circ\text{N}$ (m) and $30^\circ\text{N}\text{--}60^\circ\text{N}$ (n) regions, the trend of DMS with pCO_2 changes is not significant ($P > 0.1$), indicating that these results are not suitable for regional constraints. Future research demands a richer dataset of observations and an expanded range of parameters influencing the mechanisms behind pCO_2 and DMS responses to explore variations at various spatial scales.

This study employed an offline approach to modify the simulated DMS concentration results from ESMs. Incorporating the pCO_2 -dependent constraint parameterization derived from our research into ESMs and conducting oceanic DMS simulations through online methods could potentially produce more accurate outcomes. In addition, further advancements in laboratory experiment results regarding the pCO_2 (pH) and DMS relationship may also guide updates in parameterization schemes.

METHODS

Description of Global Observational Datasets and ESMs

The global observational datasets utilized in this study were sourced from The Surface Ocean CO_2 Atlas³⁶ and the Global Surface Seawater DMS Database³⁷, respectively. In total, there were 30,568,073 and 88,786 valid measurements for seawater pCO_2 (1957–2020) and sea-surface DMS concentrations (1972–2017). We matched these two datasets since the longitude and latitude of pCO_2 and DMS measurements are equal in decimal place, and simultaneously the sampling date should be equal in hour scale. For example, both of pCO_2 and DMS sampling geographical coordinates and date are 55.1°N , 150.2°E and 1 October, 2010, 17:00, we assumed that the pCO_2 and DMS were from the same sampling site at the same time. After removing duplicates, we got a total of 11,617 pairs for pCO_2 and DMS (Supplementary Fig. 1), which cover a time span from 1987 to 2015 (28 years). The minimum and maximum values of pCO_2 are 110.7 and 695.1 μatm , to eliminate the “noise” from low-frequency variation of measurements below a given space and timescale³⁸, data from each 5 μatm interval within 100 to 700 μatm (100–105, 106–110, ..., 696–700) were averaged and log-transformed.

In this study, four state-of-the-art CMIP6 ESMs (CNRM-ESM2-1²⁷, MIROC-ES2L²⁹, NorESM2-LM¹⁷, and UKESM1-0-LL²⁸) were utilized to evaluate the future trends in global sea-surface concentrations. Previous study³⁹ has indicated the capability of these ESMs to simulate the prominent large-scale characteristics of ocean circulation. The analysis focused on monthly sea-surface DMS concentration and the NPP outputs labeled “r1i1p1f1” and “r1i1p1f2” from CMIP6 historical and SSP585 scenario experiments. Notably, MIROC-ES2L and UKESM1-0-LL employed empirical parameterizations using chlorophyll and relevant variables to estimate DMS concentrations, while CNRM-ESM2-1 and NorESM2-LM incorporated prognostic models accounting for marine biota. All model datasets were obtained from Earth System Grid

Federation (ESGF) nodes, with further details on key characteristics provided in Supplementary Table 1.

Simulation details

We conducted simulations of aerosol size, number, and mass concentrations using the GEOS-Chem version 13.2.0 coupled with the TwO-Moment Aerosol Sectional (TOMAS) model⁴⁰. TOMAS was used to model aerosol microphysics processes, which tracks the total aerosol particle number and the mass of each aerosol species (sulfate, hydrophilic and hydrophobic organic carbon, externally and internally mixed elemental carbon, mineral dust, sea salt, and aerosol water) across 15 logarithmically size bins (from 3 nm to $10\ \mu\text{m}$)^{41,42}. GEOS-Chem-TOMAS has detailed hydrocarbon—nitrogen oxide—ozone-volatile organic compounds - bromine oxides tropospheric chemistry⁴³ and a wet and dry deposition scheme for aerosols and gas species^{44–46}. Aerosol species were fully coupled to gas-phase chemistry^{47–49}, with the ISORROPIA II scheme to calculate the thermodynamic equilibrium between inorganic aerosols and their gas-phase precursors⁵⁰. To estimate the top-of-atmosphere (TOA) all-sky direct radiative forcing (DRF) and cloud-albedo indirect radiative forcing (IRF), we utilized the Rapid Radiative Transfer Model for Global Climate Models (RRTMG)⁵¹. For the DRF, we calculated aerosol optical properties using GEOS-Chem-TOMAS output aerosol mass concentrations. These aerosol optical properties and monthly mean albedo and cloud fraction as input to drive the offline RRTMG model to calculate DRF with an external mixing assumption of the aerosol species. For the cloud-albedo IRF, we calculated cloud droplet number concentration following the activation parameterization from ref. ⁵². Then we used RRTMG to calculate the changes of TOA radiative flux from the changes affect cloud drop radii based on the perturbation method used in previous studies^{53,54}. More details about the implementation of RRTMG in GEOS-Chem-TOMAS are described in ref. ⁵³.

To investigate the potential changes in atmospheric DMS concentrations and its oxidation products in the future, we employed the meteorology, emissions, and boundary conditions from the Global Change and Air Pollution (GCAP 2.0) model⁵⁵ to drive GEOS-Chem-TOMAS. The GCAP 2.0 framework allows GEOS-Chem to utilize meteorology data archived from CMIP6 ESMs. Our simulations were conducted at a horizontal grid resolution of $2^\circ \times 2.5^\circ$ and 40 vertical layers. The initial conditions were obtained by performing spin-up simulations for 19 years (2040–2049, 2090–2098) to achieve a chemistry-climate steady state for the year 2099.

DATA AVAILABILITY

The pCO_2 observations data are available from The Surface Ocean CO_2 Atlas (SOCAT) (<https://www.socat.info/>). The DMS observations data are available from <http://saga.pmel.noaa.gov/dms/>. The satellite-derived chlorophyll concentrations were obtained from monthly L3-binned satellite products of MODIS-Aqua (4 km resolution), accessible at <https://oceancolor.gsfc.nasa.gov/l3/>. The GCAP2.0 meteorology data are available at <http://atmos.earth.rochester.edu/input/gc/ExtData/>⁵⁵. Model output from CMIP6 models' data are available from the Earth System Grid Federation (ESGF) and available online at <https://esgf-node.lln.gov/projects/cmip6>. The global seawater DMS concentration dataset predicted in this study are available from the corresponding authors upon reasonable request.

CODE AVAILABILITY

The GEOS-Chem model code is available at <https://doi.org/10.5281/zenodo.5500536>. The source codes for the analysis of this study are available from the corresponding author upon reasonable request.

Received: 4 June 2023; Accepted: 1 January 2024;

Published online: 12 January 2024

REFERENCES

- Charlson, R. J., Lovelock, J. E., Andreae, M. O. & Warren, S. G. Oceanic phytoplankton, atmospheric sulphur, cloud albedo and climate. *Nature* **326**, 655–661 (1987).
- Andreae, M. O. Ocean-atmosphere interactions in the global biogeochemical sulfur cycle. *Mar. Chem.* **30**, 1–29 (1990).
- Andreae, M. O. & Rosenfeld, D. Aerosol–cloud–precipitation interactions. Part 1. The nature and sources of cloud-active aerosols. *Earth-Sci. Rev.* **89**, 13–41 (2008).
- Quinn, P. K. & Bates, T. S. The case against climate regulation via oceanic phytoplankton sulphur emissions. *Nature* **480**, 51–56 (2011).
- IPCC. In *Climate Change 2021, the Physical Science Basis*. Contribution of Working Group I to the Sixth Assessment Report of the Intergovernmental Panel on Climate Change (eds Masson-Delmotte, V. et al.) <https://doi.org/10.1017/9781009157896> (Cambridge University Press, United Kingdom and New York, NY, USA, 2021) In press.
- Park, K. T. et al. Observational evidence for the formation of DMS-derived aerosols during Arctic phytoplankton blooms. *Atmos. Chem. Phys.* **17**, 9665–9675 (2017).
- Kerrison, P., Suggett, D. J., Hepburn, L. J. & Steinke, M. Effect of elevated pCO₂ on the production of dimethylsulphoniopropionate (DMSP) and dimethylsulphide (DMS) in two species of *Ulva* (Chlorophyceae). *Biogeochemistry* **110**, 5–16 (2012).
- Bénard, R. et al. Impact of anthropogenic pH perturbation on dimethyl sulfide cycling: a peek into the microbial black box. *Elem. Sci. Anth.* **9**, 00043 (2021).
- Zhang, M. et al. Characteristics of the surface water DMS and pCO₂ distributions and their relationships in the Southern Ocean, southeast Indian Ocean, and northwest Pacific Ocean. *Glob. Biogeochem. Cycles* **31**, 1318–1331 (2017).
- Hopkins, F. E. et al. The impacts of ocean acidification on marine trace gases and the implications for atmospheric chemistry and climate. *Proc. Math. Phys. Eng.* **476**, 20190769 (2020).
- Hopkins, F. E. et al. Ocean acidification and marine trace gas emissions. *Proc. Natl. Acad. Sci. USA* **107**, 760–765 (2010).
- Deng, X., Chen, J., Hansson, L.-A., Zhao, X. & Xie, P. Eco-chemical mechanisms govern phytoplankton emissions of dimethylsulfide in global surface waters. *Natl. Sci. Rev.* **8**, 4–11 (2020).
- Archer, S. D. et al. Contrasting responses of DMS and DMSP to ocean acidification in Arctic waters. *Biogeosciences* **10**, 1893–1908 (2013).
- Webb, A. L. et al. Ocean acidification has different effects on the production of dimethylsulfide and dimethylsulphoniopropionate measured in cultures of *Emiliania huxleyi* and a mesocosm study: a comparison of laboratory monocultures and community interactions. *Environ. Chem.* **13**, 314–329 (2016).
- Arnold, H. E., Kerrison, P. & Steinke, M. Interacting effects of ocean acidification and warming on growth and DMS-production in the haptophyte coccolithophore *Emiliania huxleyi*. *Glob. Chang. Biol.* **19**, 1007–1016 (2013).
- Six, K. D. et al. Global warming amplified by reduced sulphur fluxes as a result of ocean acidification. *Nat. Clim. Change* **3**, 975–978 (2013).
- Seland, Ø. et al. Overview of the Norwegian Earth System Model (NorESM2) and key climate response of CMIP6 DECK, historical, and scenario simulations. *Geosci. Model Dev.* **13**, 6165–6200 (2020).
- Tjiputra, J. F. et al. Ocean biogeochemistry in the Norwegian Earth System Model version 2 (NorESM2). *Geosci. Model Dev.* **13**, 2393–2431 (2020).
- Jiang, L.-Q. et al. Global surface ocean acidification indicators from 1750 to 2100. *J. Adv. Model. Earth Syst.* **15**, e2022MS003563 (2023).
- Bock, J. et al. Evaluation of ocean dimethylsulfide concentration and emission in CMIP6 models. *Biogeosciences* **18**, 3823–3860 (2021).
- Eyring, V. et al. Overview of the Coupled Model Intercomparison Project Phase 6 (CMIP6) experimental design and organization. *Geosci. Model Dev.* **9**, 1937–1958 (2016).
- O'Neill, B. C. et al. The Scenario Model Intercomparison Project (ScenarioMIP) for CMIP6. *Geosci. Model Dev.* **9**, 3461–3482 (2016).
- Jickells, T. D. et al. A reevaluation of the magnitude and impacts of anthropogenic atmospheric nitrogen inputs on the ocean. *Glob. Biogeochem. Cycles* **31**, 289–305 (2017).
- Wang, R. et al. Influence of anthropogenic aerosol deposition on the relationship between oceanic productivity and warming. *Geophys. Res. Lett.* **42**, 10745–10754 (2015).
- Wang, W. L. et al. Global ocean dimethyl sulfide climatology estimated from observations and an artificial neural network. *Biogeosciences* **17**, 5335–5354 (2020).
- Kwiatkowski, L. et al. Twenty-first century ocean warming, acidification, deoxygenation, and upper-ocean nutrient and primary production decline from CMIP6 model projections. *Biogeosciences* **17**, 3439–3470 (2020).
- Séférian, R. et al. Evaluation of CNRM Earth System Model, CNRM-ESM2-1: role of earth system processes in present-day and future climate. *J. Adv. Model. Earth Syst.* **11**, 4182–4227 (2019).
- Sellar, A. A. et al. Implementation of U.K. Earth System Models for CMIP6. *J. Adv. Model. Earth Syst.* **12**, e2019MS001946 (2020).
- Hajima, T. et al. Development of the MIROC-ES2L Earth system model and the evaluation of biogeochemical processes and feedbacks. *Geosci. Model Dev.* **13**, 2197–2244 (2020).
- Aranami, K. & Tsunogai, S. Seasonal and regional comparison of oceanic and atmospheric dimethylsulfide in the northern North Pacific: dilution effects on its concentration during winter. *J. Geophys. Res. Atmos.* **109**, D12303 (2004).
- Hayashida, H. et al. Spatiotemporal variability in modeled bottom ice and sea surface dimethylsulfide concentrations and fluxes in the Arctic during 1979–2015. *Glob. Biogeochem. Cycles* **34**, e2019GB006456 (2020).
- Ramnarine, E. et al. Effects of near-source coagulation of biomass burning aerosols on global predictions of aerosol size distributions and implications for aerosol radiative effects. *Atmos. Chem. Phys.* **19**, 6561–6577 (2019).
- Woodhouse, M. T., Mann, G. W., Carslaw, K. S. & Boucher, O. Sensitivity of cloud condensation nuclei to regional changes in dimethyl-sulphide emissions. *Atmos. Chem. Phys.* **13**, 2723–2733 (2013).
- Zhao, J. et al. Simulating the radiative forcing of oceanic dimethylsulfide (DMS) in Asia based on machine learning estimates. *Atmos. Chem. Phys.* **22**, 9583–9600 (2022).
- McDuffie, E. E. et al. A global anthropogenic emission inventory of atmospheric pollutants from sector- and fuel-specific sources (1970–2017): an application of the Community Emissions Data System (CEDS). *Earth Syst. Sci. Data* **12**, 3413–3442 (2020).
- Bakker, D. C. E. et al. A multi-decade record of high-quality fCO₂ data in version 3 of the Surface Ocean CO₂ Atlas (SOCAT). *Earth Syst. Sci. Data* **8**, 383–413 (2016).
- Lana, A. et al. An updated climatology of surface dimethylsulfide concentrations and emission fluxes in the global ocean. *Glob. Biogeochem. Cycles* **25**, GB1004 (2011).
- Gali, M., Levasseur, M., Devred, E., Simó, R. & Babin, M. Sea-surface dimethylsulfide (DMS) concentration from satellite data at global and regional scales. *Biogeosciences* **15**, 3497–3519 (2018).
- Séférian, R. et al. Tracking improvement in simulated marine biogeochemistry between CMIP5 and CMIP6. *Curr. Clim. Change Rep.* **6**, 95–119 (2020).
- Adams, P. J. & Seinfeld, J. H. Predicting global aerosol size distributions in general circulation models. *J. Geophys. Res. Atmos.* **107**, AAC 4-1–AAC 4-23 (2002).
- Lee, Y. H. & Adams, P. J. A fast and efficient version of the TwO-Moment Aerosol Sectional (TOMAS) global aerosol microphysics model. *Aerosol Sci. Technol.* **46**, 678–689 (2012).
- Lee, Y. H., Pierce, J. R. & Adams, P. J. Representation of nucleation mode microphysics in a global aerosol model with sectional microphysics. *Geosci. Model Dev.* **6**, 1221–1232 (2013).
- Pai, S. J. et al. An evaluation of global organic aerosol schemes using airborne observations. *Atmos. Chem. Phys.* **20**, 2637–2665 (2020).
- Wang, Y., Jacob, D. J. & Logan, J. A. Global simulation of tropospheric O₃-NO_x-hydrocarbon chemistry: 1. Model formulation. *J. Geophys. Res. Atmos.* **103**, 10713–10725 (1998).
- Wesely, M. L. Parameterization of surface resistances to gaseous dry deposition in regional-scale numerical models. *Atmos. Environ.* **41**, 52–63 (2007).
- Amos, H. M. et al. Gas-particle partitioning of atmospheric Hg(II) and its effect on global mercury deposition. *Atmos. Chem. Phys.* **12**, 591–603 (2012).
- Pye, H. O. T. et al. Effect of changes in climate and emissions on future sulfate-nitrate-ammonium aerosol levels in the United States. *J. Geophys. Res. Atmos.* **114**, 138385 (2009).
- Alexander, B. et al. Sulfate formation in sea-salt aerosols: constraints from oxygen isotopes. *J. Geophys. Res. Atmos.* **110**, D10307 (2005).
- Park, R. J., Jacob, D. J., Field, B. D., Yantosca, R. M. & Chin, M. Natural and trans-boundary pollution influences on sulfate-nitrate-ammonium aerosols in the United States: implications for policy. *J. Geophys. Res. Atmos.* **109**, D15204 (2004).
- Fountoukis, C. & Nenes, A. ISORROPIA II: a computationally efficient thermodynamic equilibrium model for K⁺-Ca²⁺-Mg²⁺-NH₄⁺-Na⁺-SO₄²⁻-NO₃⁻-Cl⁻-H₂O aerosols. *Atmos. Chem. Phys.* **7**, 4639–4659 (2007).
- Iacono, M. J. et al. Radiative forcing by long-lived greenhouse gases: calculations with the AER radiative transfer models. *J. Geophys. Res. Atmos.* **113**, D13103 (2008).
- Abdul-Razzak, H. & Ghan, S. J. A parameterization of aerosol activation 3. Sectional representation. *J. Geophys. Res. Atmos.* **107**, AAC 1-1–AAC 1-6 (2002).
- Kodros, J. K., Cucinotta, R., Ridley, D. A., Wiedinmyer, C. & Pierce, J. R. The aerosol radiative effects of uncontrolled combustion of domestic waste. *Atmos. Chem. Phys.* **16**, 6771–6784 (2016).
- Scott, C. E. et al. The direct and indirect radiative effects of biogenic secondary organic aerosol. *Atmos. Chem. Phys.* **14**, 447–470 (2014).

55. Murray, L. T., Leibensperger, E. M., Orbe, C., Mickley, L. J. & Sulprizio, M. GCAP 2.0: a global 3-D chemical-transport model framework for past, present, and future climate scenarios. *Geosci. Model Dev.* **14**, 5789–5823 (2021).
56. Nightingale, P. D., Liss, P. S. & Schlosser, P. Measurements of air-sea gas transfer during an open ocean algal bloom. *Geophys. Res. Lett.* **27**, 2117–2120 (2000).

ACKNOWLEDGEMENTS

This work was supported by the National Natural Science Foundation of China (42375100, 42077195), the Major Program of Shanghai Committee of Science and Technology, China (22ZR1407700), and the National Key Research and Development Program of China (2016YFA060130X).

AUTHOR CONTRIBUTIONS

J.Z. developed the method for emission estimates, ran the model, analyzed the data, and wrote the paper; Y.Z. designed and supervised the study and reviewed and revised the paper; B.S. reviewed and edited the manuscript; K.R.B. and J.R.P. guided the simulations and gave valuable comments on this paper and sharpened the writing; Y.C. reviewed and edited the manuscript. All authors commented on the manuscript.

COMPETING INTERESTS

The authors declare no competing interests.

ADDITIONAL INFORMATION

Supplementary information The online version contains supplementary material available at <https://doi.org/10.1038/s41612-024-00563-y>.

Correspondence and requests for materials should be addressed to Yan Zhang.

Reprints and permission information is available at <http://www.nature.com/reprints>

Publisher's note Springer Nature remains neutral with regard to jurisdictional claims in published maps and institutional affiliations.



Open Access This article is licensed under a Creative Commons Attribution 4.0 International License, which permits use, sharing, adaptation, distribution and reproduction in any medium or format, as long as you give appropriate credit to the original author(s) and the source, provide a link to the Creative Commons license, and indicate if changes were made. The images or other third party material in this article are included in the article's Creative Commons license, unless indicated otherwise in a credit line to the material. If material is not included in the article's Creative Commons license and your intended use is not permitted by statutory regulation or exceeds the permitted use, you will need to obtain permission directly from the copyright holder. To view a copy of this license, visit <http://creativecommons.org/licenses/by/4.0/>.

© The Author(s) 2024